

# Filterless narrowband visible photodetectors

Qianqian Lin, Ardalan Armin, Paul L. Burn\* and Paul Meredith\*

**Wavelength-selective light detection is crucial for many applications, including imaging and machine vision. Narrowband spectral responses are required for colour discrimination, and current systems use broadband photodiodes combined with optical filters. This approach increases the architectural complexity and limits the quality of colour sensing. Here we report a method for tuning the spectral response to give filterless, narrowband red, green and blue photodiodes. The devices have simple planar junction architectures with the photoactive layer being a solution-processed mixture of either an organohalide perovskite or lead halide semiconductor and an organic (macro)molecule. The organic (macro)molecules modify the optical and electrical properties of the photodiode and facilitate charge collection narrowing of the device's external quantum efficiency. These red, green and blue photodiodes all possess full-width at half-maxima of <100 nm and performance metrics suitable for many imaging applications.**

Photodetectors are the mainstay of imaging systems, environmental surveillance, communications and biological sensing<sup>1–4</sup>. In general, photodetectors can be classified as spectrally broadband<sup>5–7</sup> or narrowband<sup>8–10</sup> depending on the width of their spectral response window. Spectral discrimination in state-of-the-art commercial photodetectors is currently realized using broadband inorganic semiconductor photodiodes in combination with a dichroic prism or set of optical filters<sup>11–13</sup>. However, this approach increases the photodetector architectural complexity and cost, and is a major limitation in achieving higher pixel densities in imaging systems<sup>12,14</sup>. Furthermore, the use of input filtering creates additional optical interfaces, decreases the image sharpness, negatively impacts colour constancy and also imposes ultraviolet-stability challenges<sup>12,15,16</sup>. These problems are the main motivations for finding new ways to achieve narrowband light detection without the need for input optical filtering.

A number of alternative strategies are emerging for colour discrimination, including: (1) the use of truly narrowband absorbers such as organic semiconductors and nanocrystals<sup>17–19</sup> in the photodiode active layer; (2) splitting the light into its component colours<sup>9</sup>; and (3) optical manipulation of light absorption within the active layer<sup>12</sup>. These approaches are yet to demonstrate an appropriate set of performance metrics for any meaningful application, that is, spectrally tunable narrowband responses with full-width at half-maxima (FWHM) of <100 nm, in combination with low noise, high speed and large linear dynamic range<sup>10</sup>. Recently, Armin and colleagues established a method for achieving narrowband spectral responses in red and near-infrared (NIR) photodiodes by using broadband absorbing organic semiconductors<sup>10</sup>. This method was based on manipulating the internal quantum efficiency (IQE) of the photodiode via charge collection narrowing (CCN). Paradoxically, the CCN concept uses the relatively poor charge transport properties of organic semiconductors in thick bulk heterojunction photodiodes. These devices are engineered such that only volume-generated photocarriers are collected and hence produce current. Volume photogeneration occurs for incident light energies around the optical gap of the junction material combination (a blend acceptor and donor organic semiconductors) and delivers a narrow IQE in the tail of the optical absorption. Although, in principle, manipulating the electro-optics in this way is a generic, architecturally driven approach,

the implementation of CCN still relies on having materials with the appropriate optical gap, absorption and electrical transport properties. These considerations have so far limited this promising concept to red and NIR narrowband organic semiconductor photodiodes.

In this Article we report narrowband red, green and blue photodiodes, all with FWHM < 100 nm. This is achieved using the CCN concept in organohalide perovskites and mixed lead halide semiconductors where we engineer two absorption onsets controlled by varying the blend ratio of the halides in the semiconductors<sup>20–22</sup> and/or by the addition of an organic (macro)molecule in the film to form a composite junction. In so doing we have been able to simultaneously control the optical and electrical transport properties of the photodiode and produce a unique set of fully tunable narrowband responses across the entire visible spectrum and into the NIR.

## Charge collection narrowed photodiodes

The working principles of the CCN concept have been discussed in detail by Armin and co-authors<sup>10</sup>. We reiterate the basic principles here for clarity and particularly point out the current limitations of CCN photodiodes. Consider first the simplest photodiode architecture, shown in the inset of Fig. 1, which comprises a photoactive layer (the junction) sandwiched between a transparent anode (indium tin oxide (ITO)/poly(3,4-ethylenedioxythiophene):poly(styrene sulphonate) (PEDOT:PSS)) and cathode stack (C<sub>60</sub>/LiF/Ag). The PEDOT:PSS and C<sub>60</sub> are typical materials used to engineer efficient hole and electron extraction and suppress dark current in organic<sup>7,10</sup> and the first organohalide perovskite broadband photodiodes<sup>23</sup>. In such a simple architecture, CCN is realized because the junction is optically and electrically 'thick'; that is, it has a high optical density and long transit time for photogenerated carrier extraction. The principle is demonstrated for a hypothetical junction with absorption coefficient  $\alpha$  (Fig. 1) that has two distinctly different absorption regimes: high  $\alpha$ , where the incident light intensity falls off exponentially within the junction (the Beer–Lambert regime), and low  $\alpha$ , where the incident light propagates within the junction and is subject to interference (the cavity regime). In the Beer–Lambert regime, photogenerated carriers are produced in the vicinity of the transparent conducting electrode and we term this 'surface generation'. In the cavity regime, photogenerated carriers are produced

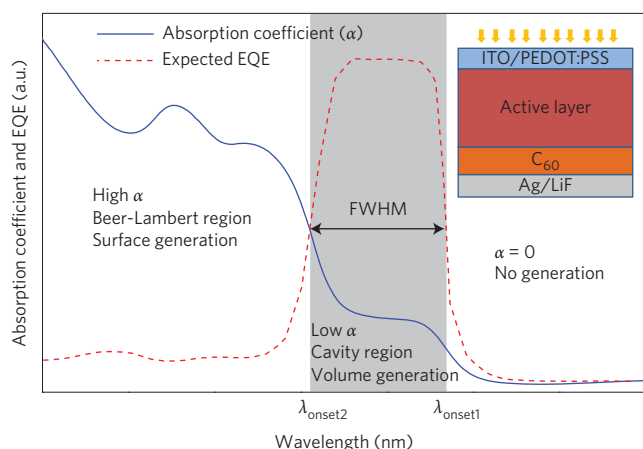


**Figure 1 | Working principles of CCN photodiodes.** The absorption coefficient profile of an active layer of defined thickness with separate high and low absorption ( $\alpha$ ) regions (solid blue line). In the high- $\alpha$  region, the Beer-Lambert law dominates the light absorption, and carriers are mainly generated near the transparent electrode (we term this ‘surface generation’). This increases the recombination and reduces the charge collection efficiency  $\eta_{\text{coll}}$  due to strongly imbalanced electron/hole transport. In the low- $\alpha$  region, cavity effects influence the light absorption significantly for optically thick junctions, and carriers are generated in the volume of the active layer (‘volume generation’). The EQE can be shaped by manipulating  $\eta_{\text{coll}}$ , that is, the IQE<sup>10</sup>. The FWHM can be controlled by tuning the two onsets of  $\alpha$  (reported as  $\text{FWHM} \approx \lambda_{\text{onset1}} - \lambda_{\text{onset2}}$ ). Inset: the simple homojunction photodiode structure, comprising a photoactive layer and interlayers between the cathode and anode.

throughout the junction, including in the vicinity of the metallic electrode, and we term this ‘volume generation’.

Comparing these two cases, the surface-generated carriers will be subject to significant recombination losses due to the higher local carrier concentration and imbalanced transit times for the electrons and holes. Thus, the charge collection efficiency  $\eta_{\text{coll}}$  is suppressed, resulting in a low (if not zero) external quantum efficiency (EQE, dashed line in Fig. 1) in the Beer-Lambert region. Recombination losses will be lower for volume-generated carriers, and the EQE is maintained in the cavity regime. For wavelengths longer (photons lower in energy) than the optical gap of the junction, the absorption coefficient decreases to zero sharply and the photoresponse vanishes. Finally, if two absorption onsets can be engineered as shown in Fig. 1, then the narrowband response can be optimized and completely controlled via the CCN electro-optical mechanism. The width of the response window is typically reported as  $\text{FWHM} \approx \lambda_{\text{onset1}} - \lambda_{\text{onset2}}$ .

It is worth noting that this theoretical optimization using two relatively sharp absorption onsets has not been considered before, the closest example being the aforementioned narrowband red and NIR bulk heterojunction (BHJ) organic photodiodes reported recently by Armin and co-authors<sup>10</sup>. In this case, the position of the peak response ( $\lambda_{\text{max}}$ ) and window (FWHM) are defined by the relatively diffuse optical gap of the bulk heterojunction organic semiconductor blend. This is currently limited by the gap of the fullerene (electron acceptor) component at  $\sim 700$  nm. Thus, blue, green or yellow narrowband CCN organic semiconductor photodiodes, which are required for full colour imaging, have remained a substantial challenge. Furthermore, the broadness of the absorption edge due to energetic disorder in organic semiconductors<sup>24</sup> makes it difficult to deliver the sharp response onsets and narrow FWHM required for filter-free discriminative colour sensing. Hence, new photoactive materials with tunable optical and electrical properties and efficient charge generation quantum

yield are required to overcome these limitations and thus demonstrate the generic power of the CCN concept over the entire red-green-blue (RGB) spectral range.

### Tunable photoactive layers

Organohalide lead perovskites have recently emerged as high-efficiency photovoltaic materials with power conversion efficiencies (PCEs) as high as 20%<sup>25–28</sup>. These hybrid semiconductors exhibit optoelectronic properties similar to those of typical inorganic direct-bandgap materials, notably the following: high charge carrier mobility; long electron and hole diffusion lengths; high dielectric constant; low electron-hole binding energy; and large absorption coefficient<sup>29–31</sup>. In addition, they can be solution-processed<sup>32,33</sup> and possess optical gap tunability<sup>20–22</sup>, similar to organic semiconductors. The field of organohalide perovskite photovoltaics has rapidly expanded to other optoelectronic platforms, in particular light sensing<sup>23</sup> and even light emission<sup>20</sup>. With respect to light sensing, properties such as high carrier generation quantum yield (delivering high specific detectivities), low recombination losses (resulting in a large linear dynamic range<sup>23</sup>) and high charge carrier mobilities (resulting in a high response frequency<sup>23,34</sup>) are very attractive features. Broadband organohalide perovskite photodetectors based on photoresistors<sup>35,36</sup> and transistors<sup>37</sup> have been realized with excellent sensitivity. More recently, high-detectivity and high-speed organohalide perovskite broadband photodiodes have been reported by a few groups<sup>23,34,38–40</sup>. In all cases, these devices rely on the broad absorption of organohalide lead perovskites.

The optical gap of organohalide lead perovskites can be tuned over a broad range by changing the blend ratio of the constituent halides—iodide/bromide/chloride<sup>21,22</sup>. Figure 2a presents absorption spectra for iodide/bromide mixed-halide materials ( $\text{CH}_3\text{NH}_3\text{PbI}_{3-x}\text{Br}_x$ ) with varying halide ratios to demonstrate the principle. This tunability can be used to deliver the necessary control over  $\lambda_{\text{onset1}}$ , but is not sufficient for realizing separate red, green and blue CCN photodiodes, which requires the shorter wavelength onset also to be manipulated ( $\lambda_{\text{onset2}}$ ). However, if both absorption onsets could be controlled then the task of using CCN to achieve a narrowband spectral response is reduced to achieving the appropriate electrical properties in the junction, that is, differentiation between volume and surface photocarrier generation as demonstrated for organic semiconductor photodiodes. We will return to this particular challenge later. To control the shorter wavelength absorption onset we found that the introduction of compatible organic (macro)molecules to form composite films could be used to engineer  $\lambda_{\text{onset2}}$ . An example of how this approach and combination of materials can be used to produce a narrowband red response is shown in Fig. 2b for the case of  $\text{CH}_3\text{NH}_3\text{PbI}_2\text{Br}$  doped with Rhodamine B (approximate concentration of  $\sim 7$  wt% calculated from its molar concentration of 0.09 M in the precursor, as described in the Methods). We will discuss this combination as an exemplar of the principle. In this composite film the  $\text{CH}_3\text{NH}_3\text{PbI}_2\text{Br}$  provides a  $\lambda_{\text{onset1}}$  at 700 nm. A clear  $\lambda_{\text{onset2}}$  then emerges at  $\sim 610$  nm, and below that wavelength the absorption coefficient of the film is a combination of the Rhodamine B and perovskite. Critically, the X-ray diffraction (XRD) spectra of the composite film shown in Fig. 2c demonstrate that the tetragonal crystal structure of the  $\text{CH}_3\text{NH}_3\text{PbI}_2\text{Br}$  is preserved when mixed with the Rhodamine B. However, the inclusion of Rhodamine B was found to decrease the crystal size and improve the film quality, as indicated by the width of the XRD peaks in Fig. 2c and depicted in the scanning electron microscopy (SEM) images in Supplementary Fig. 1. Furthermore, high crystallinity and the tetragonal structure, which is characteristic of the organohalide perovskites, was found to be preserved for all the halide ratios studied (Supplementary Fig. 2).

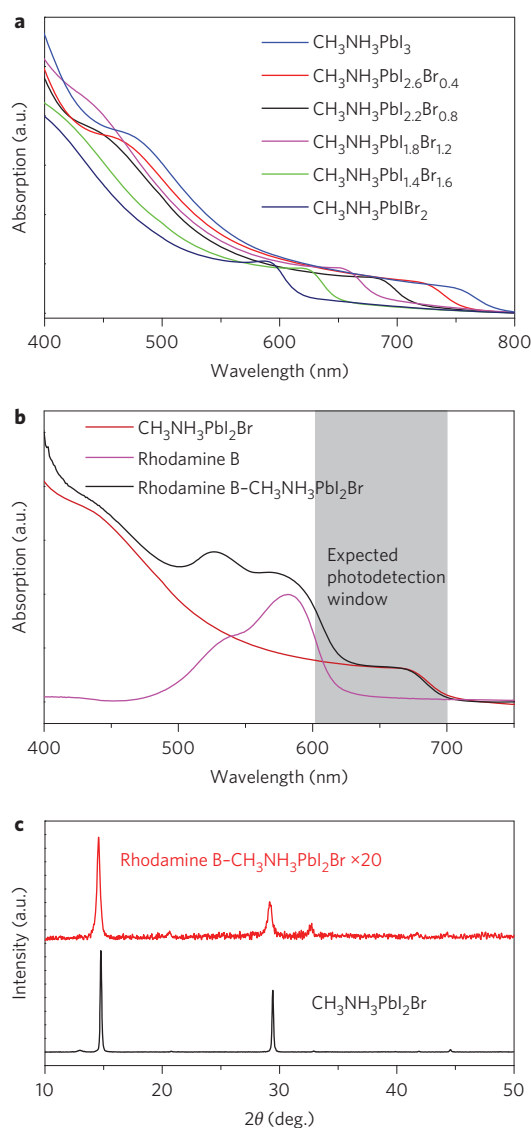


**Figure 2 | Optical gap tunability and addition of an organic molecular component to organohalide perovskite semiconductors.** **a**, The optical gap of the organohalide perovskite can be tuned by changing the ratio of  $\text{PbI}_2$  and  $\text{PbBr}_2$  during film preparation. This approach can be used to adjust absorption onset 1 ( $\lambda_{\text{onset1}}$ ) of the narrowband CCN photodiodes of Fig. 1. **b**, Addition of Rhodamine B allows absorption onset 2 ( $\lambda_{\text{onset2}}$ ) to be adjusted. **c**, Comparison of XRD spectra for organohalide perovskite ( $\text{CH}_3\text{NH}_3\text{PbI}_2\text{Br}$ ) with or without Rhodamine B. The films containing Rhodamine B possess attenuated diffraction intensity ( $\sim 20$  times lower) and broader peaks. This indicates that, by adding Rhodamine B, the growth of larger crystals is hindered and the crystal size is much smaller compared with neat organohalide perovskite films.

We now turn to the effect of the Rhodamine B on the electrical properties of the composite film. Organohalide perovskites with polycrystalline morphologies of the type utilized in high-efficiency solar cells have recently been shown to possess largely non-excitonic photocarrier generation<sup>31</sup>. Lin and colleagues<sup>31</sup> asserted that this behaviour in  $\text{CH}_3\text{NH}_3\text{PbI}_3$  is a result of a high static dielectric constant producing a low exciton binding energy. As such, at room temperature, electrons and holes are spontaneously created upon photoexcitation. However, evidence is now emerging that the local morphology (crystallite size, for example) may play a role in controlling the relative branching ratio of excitonic and non-excitonic states upon photoexcitation<sup>41</sup>.

In a system with predominantly non-excitonic dynamics, efficient charge carrier photogeneration can be delivered with no need for a bulk or linear heterostructure. The simplest possible metal–insulator–metal or (p–insulator–n) linear homojunction architectures can therefore be used to create solar cells. This is also an advantageous feature for CCN photodiodes, as it negates the need for an acceptor:donor (np) heterojunction as in the case of organic semiconductor-based devices. Figure 2b clearly shows that the fundamental optical gap of the organohalide perovskite is unaffected by the Rhodamine B in the film, which is consistent with the crystal structure. Supplementary Fig. 3 presents measurements of the static dielectric constant obtained using charge extraction with linearly increasing voltage (CELIV)<sup>42</sup>. We found the Rhodamine B- $\text{CH}_3\text{NH}_3\text{PbI}_2\text{Br}$  composite film had a static dielectric constant of 45, suggesting that the material should be largely non-excitonic and should therefore (as we show below) deliver efficient homojunction photodiodes.

### Narrowband red organohalide perovskite photodiodes

Based on the rationale outlined above, we selected a Rhodamine B: $\text{CH}_3\text{NH}_3\text{PbI}_{3-x}\text{Br}_x$  combination to deliver a narrowband red photodiode with response between  $\sim 600$  nm and  $700$  nm (defined by  $\lambda_{\text{onset2}}$  and  $\lambda_{\text{onset1}}$ , respectively). The  $700$  nm absorption edge was obtained with a precursor molar ratio of methylammonium iodide (MAI): $\text{PbI}_2$ : $\text{PbBr}_2$  of 1:0.5:0.5, resulting in  $\text{CH}_3\text{NH}_3\text{PbI}_2\text{Br}$ . By performing transfer matrix simulations (the optical constants ( $n$ ,  $k$ ) of the composite material are shown in Supplementary Fig. 4 and were obtained using spectroscopic ellipsometry according to a method we previously reported<sup>31</sup>), the optical field distribution in the photodiode junction was predicted<sup>43</sup>.

Figure 3a presents results from these transfer matrix simulations for a relatively ‘thick’ junction photodiode ( $\sim 500$  nm) for four wavelengths:  $350$  nm,  $450$  nm and  $550$  nm in the Beer–Lambert regime and  $650$  nm in the cavity regime. Based on these results, a device with an  $\sim 500$  nm junction should, at least from an optical perspective, deliver a narrowband CCN-derived response in the red. We next fabricated linear homojunction photodiodes (with the structure shown in the inset to Fig. 1) with different junction thicknesses ( $150$  nm thin to  $490$  nm thick) in order to confirm the optical findings and also test whether the electrical properties of the Rhodamine B:organohalide perovskite composite film could deliver CCN. In this regard, Fig. 3b shows EQEs at  $-0.5$  V (a typical, low operating reverse bias for photodiodes). As predicted, for the thinnest junction ( $150$  nm), all incident wavelengths cause volume carrier generation, with carriers collected with reasonable efficiency because of the relatively short extraction distance for both electrons and holes. Therefore, this device shows no colour discrimination and is effectively broadband. Increasing the junction thickness produces more surface generation for wavelengths shorter than  $\lambda_{\text{onset2}}$ . In the limit, the  $490$  nm junction delivers a sub- $100$  nm narrowband response with onsets almost precisely at the design onsets. Of particular note are the sharpness of  $\lambda_{\text{onset2}}$  and  $\lambda_{\text{onset1}}$ , the latter derived from the organohalide perovskite absorption edge, and the relatively flat EQE between  $600$  nm and  $700$  nm, corresponding to the shape of the absorption in that region (Fig. 2b). The tunability of the optical gap of the mixed-organohalide perovskites is demonstrated by the EQEs in Fig. 4a. By changing the halide ratio the narrowband response can be pushed out into the NIR, and the FWHM can also be tuned further (from  $\sim 40$  nm to  $200$  nm).

At this point, it is important to recall that the CCN mechanism originates from the recombination of surface-generated charges either geminately or non-geminately<sup>10</sup>. In efficient organohalide perovskite solar cells, the carrier mobilities are thought to be very high<sup>23,34</sup> and bimolecular recombination very low<sup>31</sup>. This means that, even in thick junctions (for example,  $500$  nm), the carrier

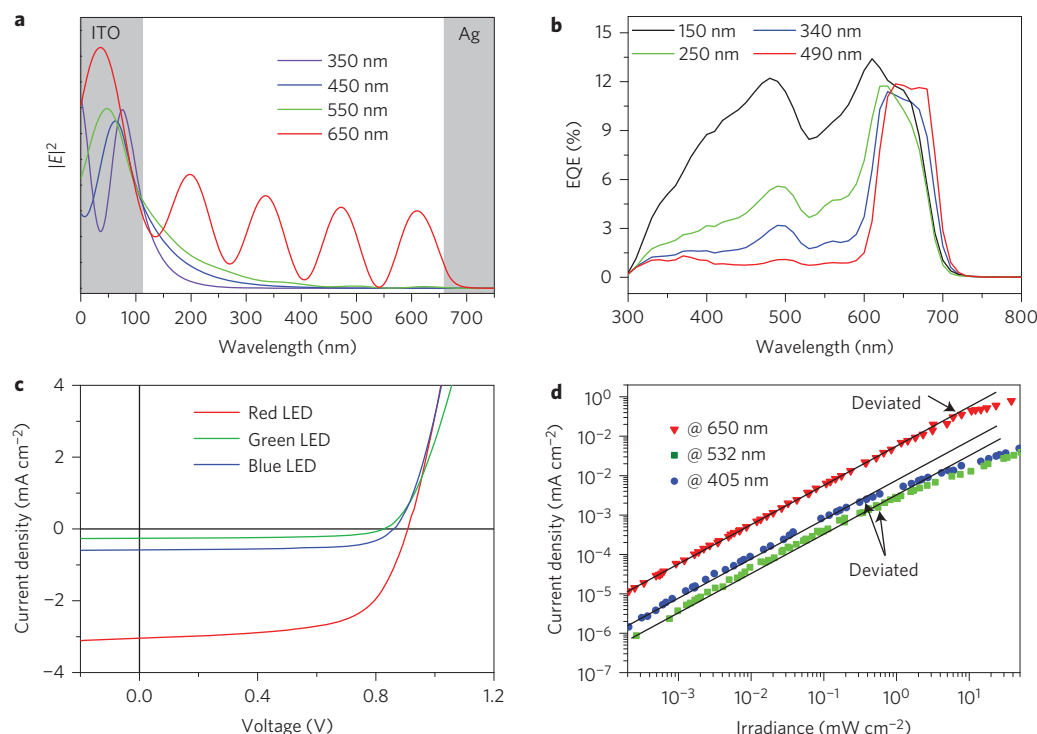


**Figure 3 | Working mechanism and performance of the red narrowband CCN photodiodes.** **a**, Optical field distributions in the red narrowband photodiodes (film thicknesses of 500 nm  $\text{CH}_3\text{NH}_3\text{PbI}_2\text{Br}$  and 60 nm  $\text{C}_{60}$ ) for four wavelengths: for  $\lambda < 600$  nm (the Beer-Lambert region) photons cannot penetrate the whole of the film and carriers are surface generated, and for  $700 \text{ nm} > \lambda > 600$  nm (the cavity region) the photocarriers are volume-generated. **b**, EQEs of narrowband red CCN photodiodes with various junction thicknesses at a reverse bias of  $-0.5$  V. The thinnest junction delivers an almost broadband response because surface- and volume-generated carriers are collected. By increasing the junction thickness, surface generation and volume generation are distinguished and the EQE at shorter wavelengths (in the Beer-Lambert region) is suppressed. **c**, Current-density-voltage ( $J$ - $V$ ) measurements of the red narrowband CCN photodiodes under different illumination colours with similar irradiances ( $\sim 50 \text{ mW cm}^{-2}$ ). All  $J$ - $V$ s show fill factors of  $\sim 50\%$ , indicating similar charge transport efficiencies for the longer-lived carriers. **d**, IPC measurements of red narrowband photodiodes (zero bias) under various irradiance intensities and three different laser wavelengths. Deviation of the photocurrent from linearity as a function of input irradiance indicates the onset of significant bimolecular recombination, which occurs at more than an order of magnitude earlier for blue and green wavelengths (surface-generated carriers).

collection efficiency  $\eta_{\text{coll}}$  is almost 100%. This would preclude the CCN mechanism because all photogenerated carriers, even those that are surface-generated, would be collected. Hence, in our thick-junction narrowband Rhodamine B: $\text{CH}_3\text{NH}_3\text{PbI}_2\text{Br}$  photodiodes, some element of the collection efficiency (mobility and/or recombination rate) has been modified. To examine these factors we first measured current density-voltage ( $J$ - $V$ ) curves for the red narrowband device under red, green and blue illumination (provided by light-emitting diode), all at an irradiance of  $\sim 50 \text{ mW cm}^{-2}$ . The results are presented in Fig. 3c, and we observe similar fill factors (FFs) of between 40 and 50% in all cases, regardless of the excitation wavelength. This implies that the transport efficiency of the long-lived carriers is maintained, but the dramatic drop in short-circuit current density for blue and green wavelengths relative to red suggests higher carrier recombination or poorer charge generation.

To further probe the recombination dynamics (and particularly the recombination order), we performed intensity-dependent photocurrent (IPC)<sup>44,45</sup> measurements—again with blue (405 nm), green (532 nm) or red (650 nm) illumination. The deviation from linearity of the IPC response has been reported to occur at the intensity (and hence carrier density) at which bimolecular recombination becomes dominant<sup>44,45</sup>. Figure 3d shows the results of these IPC measurements for the narrowband red device. Blue and green wavelengths induce deviation an order of magnitude earlier than red illumination. This confirms that higher-order non-geminate (nonlinear) recombination is present in the Beer-Lambert regime ( $\lambda < 600$  nm). Moreover, significantly lower

responsivity  $R$  in the linear regime (as seen from the offset in the logarithmic plot of Fig. 3d) for blue and green wavelengths versus red indicates the presence of higher geminate (first-order) recombination losses. These recombination results, when viewed alongside the results of Figs 2 and 3, highlight one very important feature of the composite film approach—we are able to simultaneously control the electrical and optical properties of the junction material to deliver the desired spectral response. Paradoxically, the narrowband selectivity is achieved by making the junction transport properties worse—not a common strategy in optoelectronics.

Having established the basic principles of achieving a narrowband red photodiode, we now move on to fully characterize its light detection properties. The dark current density  $J_d$  is one of the most important indicators of the noise figure of merit for photo-detectors. Figure 4b shows the measured  $J_d$  of the optimized Rhodamine B: $\text{CH}_3\text{NH}_3\text{PbI}_2\text{Br}$  composite device at  $-0.5$  V, which was  $< 5 \times 10^{-8} \text{ A cm}^{-2}$ . By measuring the noise spectral density from the Fourier transform of the current versus time (Supplementary Fig. 5), the noise current ( $i_{\text{noise}}$ ) was found to be  $\sim 100 \text{ fA Hz}^{-1/2}$  from 0 V to  $-1$  V. The noise equivalent power (NEP) can be obtained from equation (1)<sup>7</sup> and was found to be  $\sim 2 \text{ pW Hz}^{-1/2}$ .

$$\text{NEP} = \frac{i_{\text{noise}} \sqrt{B}}{R} = \frac{h c i_{\text{noise}} \sqrt{B}}{\text{EQE} e \lambda} \text{ (W)} \quad (1)$$

The specific detectivity can be calculated based on equation (1)<sup>7</sup>



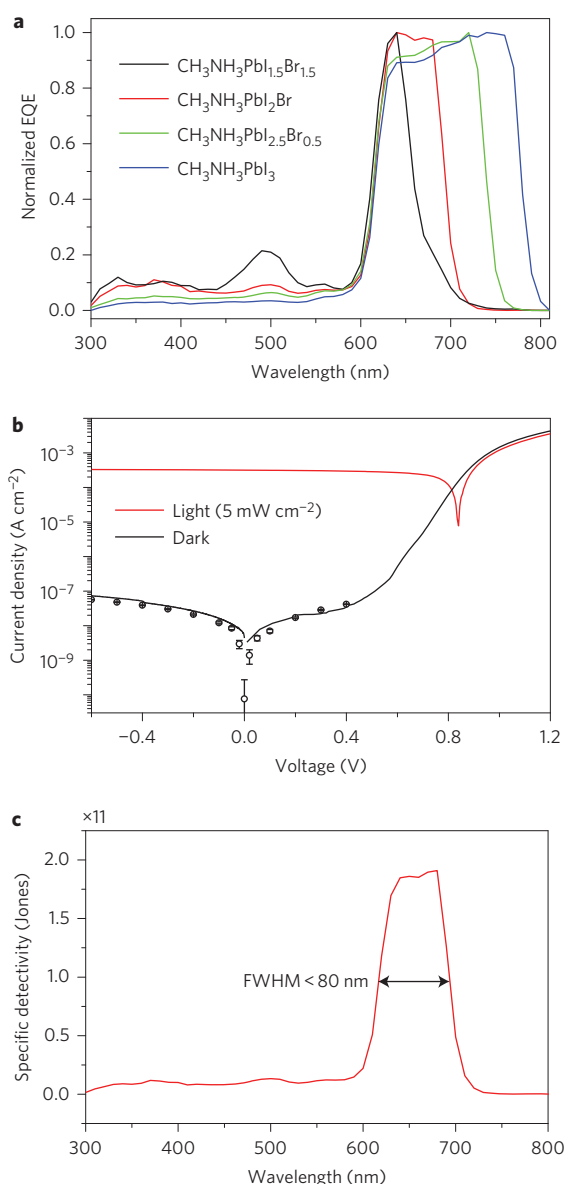


**Figure 4 | Device performance and bandwidth tunability of red narrowband photodiodes.** **a**, EQEs at  $-0.5$  V of the red narrowband photodiodes fabricated with different ratios of  $\text{PbI}_2$  and  $\text{PbBr}_2$ . The long-wavelength edge of the photoresponse window can be controlled by the semiconductor optical gap ( $\lambda_{\text{onset}}$ ). **b**, Light and dark  $J$ - $V$  curves of the devices from **a**. The dark current at  $-0.5$  V is  $<5 \times 10^{-8}$  A  $\text{cm}^{-2}$ . Each circle is an average of the measured dark current over 3 seconds with the error bars being the standard deviation. **c**, Measured specific detectivity  $D^*$  of an optimized red narrowband photodiode at  $-0.5$  V ( $1.9 \times 10^{11}$  Jones with FWHM  $<80$  nm).

from the measured noise so that

$$D^* = \frac{\sqrt{AB}}{\text{NEP}} = \frac{e\lambda\sqrt{A}\text{EQE}}{hc i_{\text{noise}}} \text{ (Hz}^{1/2} \text{ cm W}^{-1}) \quad (2)$$

where  $\lambda$  is the detection wavelength,  $e$  is the electron charge,  $A$  is the device area (here  $0.2 \text{ cm}^2$ ),  $h$  is Planck's constant and  $c$  is the speed of light in vacuum. The calculated  $D^*$  at the detection frequency of the EQE (120 Hz) is shown in Fig. 4c, with values reaching  $\sim 2 \times 10^{11}$  Jones ( $\text{Hz}^{1/2} \text{ cm W}^{-1}$ ) in the photodiode response window. Overall, these performance metrics compare very favourably with state-of-the-art narrowband filter-based visible-light

photodetectors but with far superior tunability, FWHM and photo-response suppression outside the design window. It is also worth noting that these red narrowband photodiodes were actually quite stable, contrary to current expectations of organohalide perovskite devices. Using basic encapsulation techniques (see Methods), the photodiodes maintained their performance after four months stored in air, surviving more than twenty measurement sets during that time. Example EQEs are shown in Supplementary Fig. 6. Given the supposed instabilities of organohalide perovskites, this is promising from a real application perspective.

### Blue and green narrowband photodiodes

The principles outlined for red narrowband photodiodes can be extended to the blue and green regions of the visible spectrum. The same challenges exist: finding materials to deliver appropriate and tunable absorption onsets and controlling the junction recombination dynamics. Clearly, Rhodamine B, given the position of its absorption onset ( $\sim 630$  nm), is not appropriate, and for blue and green devices we used PEIE (polyethylenimine, 80% ethoxylated) to deliver composite films with the appropriate properties. There is a subtle difference between the roles of Rhodamine B in the red photodiodes and PEIE in the green and blue photodiodes. In the latter, absorption onsets can be solely adjusted by changing the halide ratio in the semiconductor. PEIE only absorbs in the ultra-violet and hence does not play an optical role—it is used to manipulate the crystallite size and overall degree of disorder and hence control the junction electrical properties to realize CCN.

From Fig. 2a it can be seen that an appropriate mixed-organohalide perovskite ( $\text{CH}_3\text{H}_3\text{PbI}_x\text{Br}_{3-x}$ ) could deliver the correct  $\lambda_{\text{onset}}$  for a green photodiode, but not shorter wavelengths. To realize a blue device we used a mixed-lead-halide system ( $\text{PbI}_x\text{Br}_{2-x}$ ) and tuned the optical gap by controlling the ratio of  $\text{PbI}_2$  and  $\text{PbBr}_2$  in the same way as for the organohalide perovskites. Addition of PEIE did not change the basic structure of the  $\text{PbI}_x\text{Br}_{2-x}$  in the composite film, although (as in the case of Rhodamine B) the crystal size decreased and there was an increase in overall disorder of the film (see XRD spectra in Supplementary Fig. 7).

Films containing PEIE and  $\text{CH}_3\text{H}_3\text{PbI}_x\text{Br}_{3-x}$  or  $\text{PbI}_x\text{Br}_{2-x}$  at the optimized ratios also had high static dielectric constants,  $\sim 35$  and  $19$ , respectively, as measured by CELIV (Supplementary Fig. 3). We could therefore realistically expect that these material combinations will also display largely non-excitonic charge-generation physics and therefore be suited to a homojunction architecture. Thus, the blue and green photodiodes were optimized in the same way as described for the red device with an identical structure. The approximate Rhodamine B and PEIE concentrations, and the halide ratios and junction thicknesses for the final RGB 'suite' of photodetectors are provided in Table 1. The precursor solution compositions to achieve these junction structures are provided in the Methods. Figure 5a presents the absorption coefficients of the red, green and blue device material combinations, and

**Table 1 | Typical organic component concentrations, compositions and junction thicknesses for the final RGB suite of photodetectors.**

Photodiodes	Organic component	Organic component concentration (wt%)	Composition	Junction thickness (nm)
Red	Rhodamine B	$\sim 7$	$\text{CH}_3\text{NH}_3\text{PbI}_2\text{Br}$	$\sim 500$ – $600$ nm
Green	PEIE	$\sim 0.75$	$\text{CH}_3\text{NH}_3\text{PbI}_2\text{Br}_2$	$\sim 500$ – $600$ nm
Blue	PEIE	$\sim 0.75$	$\text{PbI}_{1.4}\text{Br}_{0.6}$	$\sim 400$ – $500$ nm

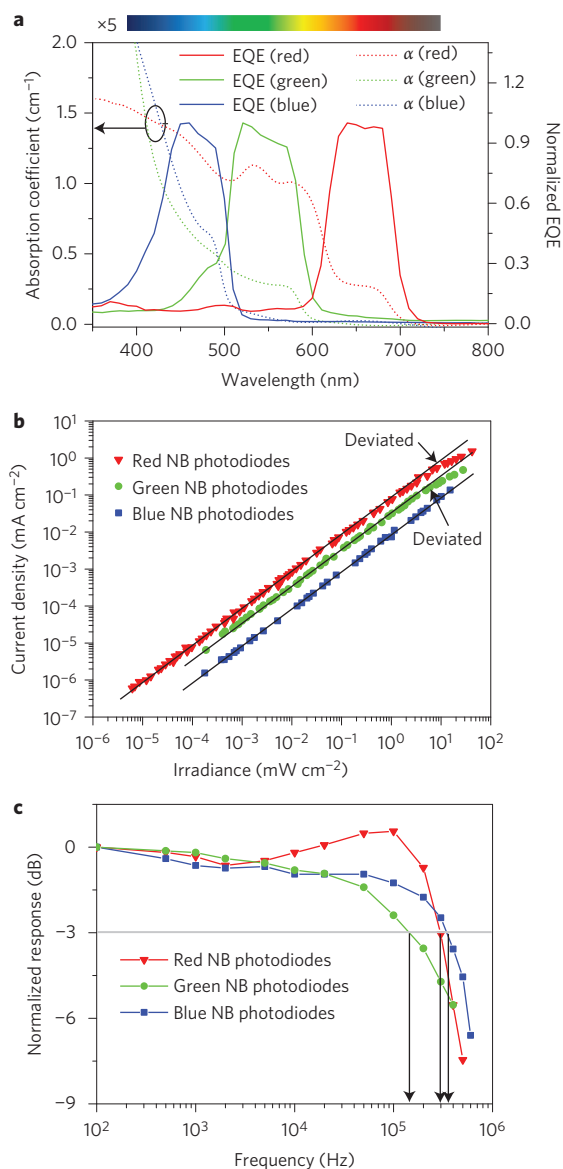


**Figure 5 | Device performance summary of red, green and blue narrowband CCM photodiodes.** **a**, EQE spectra at  $-0.5$  V of optimized narrowband photodiodes and related junction absorption coefficients clearly showing how the CCM concept can be realized across the visible spectrum. **b**, Linear dynamic range (LDR) of the optimized narrowband photodiodes measured at  $-0.5$  V. The red photodetector shows a linear response of  $>6$  orders of magnitude versus irradiance intensity, whereas the green and blue photodetectors exhibit  $\sim 5$  orders of magnitude of linear response. **c**, Frequency response (speed) of optimized narrowband RGB photodiodes at  $-0.5$  V. The green photodetector shows  $f_{-3\text{dB}} \approx 144$  kHz and the red and blue photodetectors  $f_{-3\text{dB}}$  values of  $\sim 297$  kHz and  $345$  kHz, respectively—all more than sufficient for most imaging applications. NB, narrowband.

the junctions were optimized to deliver an FWHM of  $\sim 100$  nm in the response windows  $600\text{--}700$  nm,  $500\text{--}600$  nm and  $400\text{--}500$  nm. Figure 5a also shows the normalized EQE for the RGB suite of photodetectors, confirming that the desired photoresponses were achieved and noting the blindness of each outside its designed spectral window. We also note that the exact  $\lambda_{\text{max}}$  and FWHM of the blue and green photodiodes can be further tuned by adjusting the optical gap of the semiconductor and hence  $\lambda_{\text{onset}}$ .

Supplementary Fig. 8 presents the reverse bias voltage dependence of the EQE for each of the optimized photodiodes.

Although, as previously noted, the red photodiodes show virtually no bias dependence, the blue and green devices do. This is indicative of poorer charge collection efficiencies in the latter. However, all three RGB photodetectors deliver  $>10\%$  EQE at a modest reverse bias ( $-1$  V), again advantageous from a practical point of view for applications such as cameras. The dark current densities and specific detectivities at  $\lambda_{\text{max}}$  are summarized in Supplementary Table 1. Once again we observe the superiority of the red photodiode, but note the respectable performance of the blue and green devices, which we believe are the first truly narrowband photodetectors for these spectral regions. Additional performance metrics are presented in Fig. 5b. The measured linear dynamic ranges (LDRs) at low reverse bias ( $-0.5$  V) for the red photodiode (as indicated in Fig. 3d) were over six orders of magnitude (conventionally expressed as  $\text{LDR} = 120$  dB)<sup>2,3,7</sup>, and the green and blue devices exhibited approximately five orders of magnitude of linear response. These metrics represent the state-of-the-art for any narrowband detectors.

Finally, another important metric for photodetectors is their temporal or frequency response, which defines the speed of image capture, or data acquisition rate in applications such as surveillance. The frequency response is dictated by the charge carrier transit time and the capacitance–resistance ( $RC$ ) characteristic time of the system<sup>7</sup>. Although the charge carrier transit time is expected to be extremely short in organohalide perovskites (and indeed lead halides) due to the high charge carrier mobilities<sup>23,46</sup>, their large dielectric constants increase the cell capacitance and therefore limit the response speed<sup>23</sup>. Figure 5c shows the frequency responses of the optimized photodiodes at  $-0.5$  V. The green device shows an  $f_{-3\text{dB}}$  of  $\sim 144$  kHz, and the red and blue photodiodes have a slightly higher  $f_{-3\text{dB}} = 297$  kHz and  $345$  kHz, respectively. Such frequency responses are far above the values required for imaging applications. However, we should emphasize that these frequency responses are close to the  $RC$  limited bandwidth ( $f_{\text{RC}}$ ), which can be calculated by equation (3)<sup>7</sup>:

$$(f_{\text{RC}}) = \frac{1}{2\pi RC} \text{ (Hz)} \quad (3)$$

To assess this limit, the  $RC$  time was quantified from the current density decay of the devices (an example is shown for the blue photodiode in Supplementary Fig. 9). The red, blue and green photodiodes showed  $RC = 0.4\text{--}0.7$   $\mu\text{s}$ , corresponding to  $f_{\text{RC}} = 400\text{--}200$  kHz. The measured rise times ( $t_r$ ) and fall times ( $t_f$ ) can be seen in Supplementary Fig. 8d,e,f, with  $t_r = 3.0$   $\mu\text{s}$ ,  $6.9$   $\mu\text{s}$  and  $1.8$   $\mu\text{s}$ , and  $t_f = 1.9$   $\mu\text{s}$ ,  $3.0$   $\mu\text{s}$  and  $1.5$   $\mu\text{s}$  for the red, green and blue devices, respectively. Such high-speed responses are similar to commercial broadband visible inorganic semiconductor photodiodes. However, in our current case, these values were obtained based on a device area of  $0.2$  cm<sup>2</sup>, that is, orders of magnitude larger than the pixel size required for imaging sensors. Therefore, the frequency response of these composite photodiodes could ultimately be transit-time-limited instead of  $RC$ -limited as calculated previously by Lin and colleagues<sup>23</sup> and experimentally shown by Dou and colleagues<sup>34</sup> and Fang and co-authors<sup>47</sup>.

## Conclusion

In summary, we have demonstrated the first truly narrowband, filterless set of red, green and blue photodetectors with tunable photoresponses and  $\text{FWHM} < 100$  nm. The devices use organohalide perovskites or mixed lead halides as solution-processable semiconductors. The optical and electrical properties of the photoactive films are controlled by the addition of an organic component. Two absorption onsets are engineered, with the positions determined by optical gap tuning of the semiconductor and choice of the organic (macro)molecular component of the composite film.

These onsets are sharp and establish the optical conditions for realizing CCN, with the creation of two spectral regimes, Beer–Lambert and cavity dominated. The basic crystal structure of the organohalide perovskites and mixed lead halides within a composite film are the same as in neat films of the semiconducting materials, although the crystal size is decreased and hence there is an increase in the overall film disorder. All the composite films have high static dielectric constants, suggesting they possess non-excitonic charge generation physics; that is, are suited for the simplest possible homojunction photodiode architectures. The added organic components in the composite films act to increase free carrier recombination, allowing only volume-generated carriers to be collected and thus achieving the electrical requirements for CCN. The strategy therefore relies upon making the film transport properties worse rather than better, an unusual approach in optoelectronics. The transport efficiencies of neat organohalide perovskite films of the type used in solar cells are simply too high to achieve CCN. The red, green and blue photodiodes were fully characterized and delivered state-of-the-art narrowband performance metrics: low dark current, high specific detectivities, large LDRs and fast frequency responses that will likely be transit-time- rather than RC-limited in practical applications. Critically, all the photodiodes were highly selective for their design windows, with sharp photoresponse rises and falls. This is very promising for purer illuminant-independent colour recognition and contrast. Our results further emphasize the potential of organohalide perovskites and related materials for low-cost, next-generation optoelectronics. The strategy we introduce has generic utility to control the physical, optical, chemical and processing properties of solution-processed and indeed evaporated semiconductors for multiple applications.

## Methods

Methods and any associated references are available in the [online version of the paper](#).

Received 3 May 2015; accepted 10 August 2015;  
published online 14 September 2015

## References

- Konstantatos, G. & Sargent, E. H. Nanostructured materials for photon detection. *Nature Nanotech.* **5**, 391–400 (2010).
- Gong, X. *et al.* High-detectivity polymer photodetectors with spectral response from 300 nm to 1450 nm. *Science* **325**, 1665–1667 (2009).
- Konstantatos, G., Clifford, J., Levina, L. & Sargent, E. H. Sensitive solution-processed visible-wavelength photodetectors. *Nature Photon.* **1**, 531–534 (2007).
- Baeg, K. J., Binda, M., Natali, D., Caironi, M. & Noh, Y. Y. Organic light detectors: photodiodes and phototransistors. *Adv. Mater.* **25**, 4267–4295 (2013).
- Clifford, J. P. *et al.* Fast, sensitive and spectrally tuneable colloidal-quantum-dot photodetectors. *Nature Nanotech.* **4**, 40–44 (2008).
- Guo, F., Xiao, Z. & Huang, J. Fullerene photodetectors with a linear dynamic range of 90 dB enabled by a cross-linkable buffer layer. *Adv. Opt. Mater.* **1**, 289–294 (2013).
- Armin, A. *et al.* Thick junction broadband organic photodiodes. *Laser Photon. Rev.* **8**, 924–932 (2014).
- Guo, F. *et al.* A nanocomposite ultraviolet photodetector based on interfacial trap-controlled charge injection. *Nature Nanotech.* **7**, 798–802 (2012).
- Nishiwaki, S., Nakamura, T., Hiramoto, M., Fujii, T. & Suzuki, M. Efficient colour splitters for high-pixel-density image sensors. *Nature Photon.* **7**, 240–246 (2013).
- Armin, A., Jansen-van Vuuren, R. D., Kopidakis, N., Burn, P. L. & Meredith, P. Narrowband light detection via internal quantum efficiency manipulation of organic photodiodes. *Nature Commun.* **6**, 6343 (2015).
- Lukac, R. Single-sensor imaging in consumer digital cameras: a survey of recent advances and future directions. *J. Real-time Image Proc.* **1**, 45–52 (2006).
- Park, H. *et al.* Filter-free image sensor pixels comprising silicon nanowires with selective color absorption. *Nano Lett.* **14**, 1804–1809 (2014).
- Xu, T., Wu, Y.-K., Luo, X. & Guo, L. J. Plasmonic nanoresonators for high-resolution colour filtering and spectral imaging. *Nature Commun.* **1**, 59 (2010).
- Yokogawa, S., Burgos, S. P. & Atwater, H. A. Plasmonic color filters for CMOS image sensor applications. *Nano Lett.* **12**, 4349–4354 (2012).
- Gautam, V., Bag, M. & Narayan, K. Single-pixel, single-layer polymer device as a tricolor sensor with signals mimicking natural photoreceptors. *J. Am. Chem. Soc.* **133**, 17942–17949 (2011).
- Higashi, Y., Kim, K.-S., Jeon, H.-G. & Ichikawa, M. Enhancing spectral contrast in organic red-light photodetectors based on a light-absorbing and exciton-blocking layered system. *J. Appl. Phys.* **108**, 034502 (2010).
- Lim, S.-J. *et al.* Organic-on-silicon complementary metal–oxide–semiconductor colour image sensors. *Sci. Rep.* **5**, 7708 (2015).
- Lee, K.-H. *et al.* Dynamic characterization of green-sensitive organic photodetectors using non-fullerene small molecules: frequency response based on the molecular structure. *J. Phys. Chem. C* **118**, 13424–13431 (2014).
- Lyons, D. M. *et al.* Narrow band green organic photodiodes for imaging. *Org. Electron.* **15**, 2903–2911 (2014).
- Tan, Z.-K. *et al.* Bright light-emitting diodes based on organometal halide perovskite. *Nature Nanotech.* **9**, 687–692 (2014).
- Kim, Y. H. *et al.* Multicolored organic/inorganic hybrid perovskite light-emitting diodes. *Adv. Mater.* **27**, 1248–1254 (2014).
- Kulkarni, S. A. *et al.* Band-gap tuning of lead halide perovskites using a sequential deposition process. *J. Mater. Chem. A* **2**, 9221–9225 (2014).
- Lin, Q., Armin, A., Lyons, D. M., Burn, P. L. & Meredith, P. Low noise, IR-blind organohalide perovskite photodiodes for visible light detection and imaging. *Adv. Mater.* **27**, 1969–2120 (2015).
- Benson-Smith, J. J. *et al.* Formation of a ground-state charge-transfer complex in polyfluorene/[6, 6]-phenyl-C61 butyric acid methyl ester (PCBM) blend films and its role in the function of polymer/PCBM solar cells. *Adv. Funct. Mater.* **17**, 451–457 (2007).
- Green, M. A., Ho-Baillie, A. & Snaith, H. J. The emergence of perovskite solar cells. *Nature Photon.* **8**, 506–514 (2014).
- Xiao, Z. *et al.* Giant switchable photovoltaic effect in organometal trihalide perovskite devices. *Nature Mater.* **14**, 193–198 (2014).
- Zhou, H. *et al.* Interface engineering of highly efficient perovskite solar cells. *Science* **345**, 542–546 (2014).
- Jeon, N. J. *et al.* Compositional engineering of perovskite materials for high-performance solar cells. *Nature* **517**, 476–480 (2015).
- Stranks, S. D. *et al.* Electron–hole diffusion lengths exceeding 1 micrometer in an organometal trihalide perovskite absorber. *Science* **342**, 341–344 (2013).
- Xing, G. *et al.* Long-range balanced electron- and hole-transport lengths in organic–inorganic  $\text{CH}_3\text{NH}_3\text{PbI}_3$ . *Science* **342**, 344–347 (2013).
- Lin, Q., Armin, A., Nagiri, R. C. R., Burn, P. L. & Meredith, P. Electro-optics of perovskite solar cells. *Nature Photon.* **9**, 106–112 (2014).
- Jeon, N. J. *et al.* Solvent engineering for high-performance inorganic–organic hybrid perovskite solar cells. *Nature Mater.* **13**, 897–903 (2014).
- Xiao, M. *et al.* A fast deposition–crystallization procedure for highly efficient lead iodide perovskite thin-film solar cells. *Angew. Chem. Int. Ed.* **126**, 10056–10061 (2014).
- Dou, L. *et al.* Solution-processed hybrid perovskite photodetectors with high detectivity. *Nature Commun.* **5**, 5404 (2014).
- Hu, X. *et al.* High-performance flexible broadband photodetector based on organolead halide perovskite. *Adv. Funct. Mater.* **24**, 7373–7380 (2014).
- Xia, H.-R., Li, J., Sun, W.-T. & Peng, L.-M. Organohalide lead perovskite based photodetectors with much enhanced performance. *Chem. Commun.* **50**, 13695–13697 (2014).
- Lee, Y. *et al.* High-performance perovskite–graphene hybrid photodetector. *Adv. Mater.* **27**, 41–46 (2015).
- Dong, R. *et al.* High gain and low-driving-voltage photodetectors based on organolead triiodide perovskites. *Adv. Mater.* **27**, 1912–1918 (2015).
- Li, D., Dong, G., Li, W. & Wang, L. High performance organic–inorganic perovskite–optocoupler based on low-voltage and fast response perovskite compound photodetector. *Sci. Rep.* **5**, 7902 (2015).
- Sutherland, B. R. *et al.* Sensitive, fast, and stable perovskite photodetectors exploiting interface engineering. *ACS Photon.* **2**, 1117–1123 (2015).
- Grancini, G. *et al.* Role of microstructure in the electron–hole interaction of hybrid lead halide perovskites. *Nature Photon.* <http://dx.doi.org/10.1038/nphoton.2015.151> (2015).
- Armin, A. *et al.* Balanced carrier mobilities: not a necessary condition for high-efficiency thin organic solar cells as determined by MIS-CELIV. *Adv. Energy Mater.* **4**, 1300954 (2014).
- Burkhard, G. F., Hoke, E. T. & McGehee, M. D. Accounting for interference, scattering, and electrode absorption to make accurate internal quantum efficiency measurements in organic and other thin solar cells. *Adv. Mater.* **22**, 3293–3297 (2010).
- Koster, L., Kemerink, M., Wienk, M. M., Maturová, K. & Janssen, R. A. Quantifying bimolecular recombination losses in organic bulk heterojunction solar cells. *Adv. Mater.* **23**, 1670–1674 (2011).
- Stolterfoht, M. *et al.* Photocarrier drift distance in organic solar cells and photodetectors. *Sci. Rep.* **5**, 9949 (2015).
- Leijtens, T. *et al.* Electronic properties of meso-superstructured and planar organometal halide perovskite films: charge trapping, photodoping, and carrier mobility. *ACS Nano* **8**, 7147–7155 (2014).

47. Fang, Y. & Huang, J. Resolving weak light of sub-picowatt per square centimeter by hybrid perovskite photodetectors enabled by noise reduction. *Adv. Mater.* **27**, 2804–2810 (2015).

### Acknowledgements

P.L.B. is a UQ Vice Chancellor's Research Focussed Fellow and P.M. is an ARC Discovery Outstanding Researcher Award Fellow. Q.L. is supported by an International Postgraduate Research Scholarship (IPRS). This work was performed in part at the Queensland node of the Australian National Fabrication Facility (ANFF), a company established under the National Collaborative Research Infrastructure Strategy to provide nano and micro fabrication facilities for Australia's researchers. This Program has also been supported by the Australian Government through the Australian Renewable Energy Agency (ARENA) Australian Centre for Advanced Photovoltaics. Responsibility for the views, information or advice expressed herein is not accepted by the Australian Government.

### Author contributions

Q.L. characterized the perovskite films and fabricated the devices. Q.L. and A.A. tested the devices and all authors interpreted the data. P.L.B. and P.M. supervised the project. All authors contributed to preparation of the manuscript. All authors have given approval to the final version of the manuscript.

### Additional information

Supplementary information is available in the [online version](#) of the paper. Reprints and permissions information is available online at [www.nature.com/reprints](http://www.nature.com/reprints). Correspondence and requests for materials should be addressed to P.L.B. and P.M.

### Competing financial interests

The authors declare no competing financial interests.



## Methods

**Materials.** Lead iodide ( $\text{PbI}_2$ , 99.999% trace metals basis), lead bromide ( $\text{PbBr}_2$ , 99.999% trace metals basis) and lead chloride ( $\text{PbCl}_2$ , 99.999% trace metals basis) were purchased from Sigma Aldrich. Methylammonium iodide (MAI, MS101000-10) and methylammonium bromide (MABr, MS301000-05) were purchased from Dyesol Pty Ltd. PEDOT:PSS was obtained from Heraeus (Clevios P Al4083).  $\text{C}_{60}$  was purchased from ADS. Polyethylenimine, 80% ethoxylated solution (PEIE, 37 wt% in water) and Rhodamine B (83689, for fluorescence) were purchased from Sigma Aldrich. All commercial products were used as received.

**Device fabrication.** The photodetectors were fabricated on commercial ITO-patterned glass electrodes ( $15 \Omega \text{ sq}^{-1}$ , Kintec) in a class 1000 cleanroom. The ITO electrodes were cleaned in a detergent solution (Alconox) bath at  $70^\circ\text{C}$  for 10 min, followed by sonication in sequence with Alconox, Milli-Q water, acetone and 2-propanol (IPA) for 10 min each. The cleaned substrates were dried with nitrogen before being coated with  $30 \pm 5 \text{ nm}$  PEDOT:PSS by spin-coating at 5,000 r.p.m. for 30 s. The PEDOT:PSS-coated substrates were heated on a hot plate at  $170^\circ\text{C}$  for 20 min. After cooling, the substrates were transferred to a nitrogen-filled glovebox for device fabrication ( $\text{O}_2 < 1 \text{ ppm}$ ,  $\text{H}_2\text{O} < 1 \text{ ppm}$ ).

Active layers were spin-coated onto the PEDOT:PSS layer using the following methods. The red photodetectors contained Rhodamine B and different ratios of  $\text{PbI}_2$  and  $\text{PbBr}_2$  to tune the optical gap of the mixed-halide perovskite  $\text{CH}_3\text{NH}_3\text{PbI}_x\text{Br}_{3-x}$ . Typically, the molar concentration of MAI was kept at 1 M ( $160 \text{ mg ml}^{-1}$ ). The sum of the molar concentrations of  $\text{PbI}_2$  and  $\text{PbBr}_2$  was also kept at 1 M for consistency. Thus, the ratio of  $\text{PbI}_2$  and  $\text{PbBr}_2$  (varying from 1:0, 0.75:0.25, 0.5:0.5 to 0.25:0.75) determined the optical gap of the  $\text{CH}_3\text{NH}_3\text{PbI}_x\text{Br}_{3-x}$ . The molar concentration of Rhodamine B was maintained at 0.09 M ( $\sim 7 \text{ wt\%}$ ). Independent of the  $\text{PbI}_2$ : $\text{PbBr}_2$  ratio, casting solutions were prepared in  $\gamma$ -butyrolactone and spin-coated at 1,000 r.p.m. for 120 s followed by 4,000 r.p.m. for 40 s to create the active layers.

Green photodetectors contained PEIE and different ratios of  $\text{PbI}_2$  and  $\text{PbBr}_2$  to tune the optical gap of the mixed-halide perovskite  $\text{CH}_3\text{NH}_3\text{PbI}_x\text{Br}_{3-x}$ . Typically, 469 mg  $\text{PbI}_2$  and 66 mg  $\text{PbBr}_2$  were dissolved in  $N,N$ -dimethylformamide (DMF) (1 ml) to create a 1.2 M  $\text{PbI}_{1.7}\text{Br}_{0.3}$  solution. A 37 wt% PEIE solution in deionized water was diluted by DMF to 5 wt%, and 30  $\mu\text{l}$  of this 5 wt% PEIE solution was added into 170  $\mu\text{l}$  of the  $\text{PbI}_{1.7}\text{Br}_{0.3}$  solution and stirred for 30 min. The PEIE:  $\text{PbI}_{1.7}\text{Br}_{0.3}$  solution was then spin-coated at 700 r.p.m. for 180 s onto the PEDOT:PSS pre-prepared substrates. The films were then dipped into a 15  $\text{mg ml}^{-1}$  MABr IPA solution for 15 min, during which the colour of the film gradually changed from yellow to red. The films were rinsed with IPA to remove excess MABr. The perovskite composition within the composite film was estimated from the optical gap ( $\sim 600 \text{ nm}$ ) to be  $\text{CH}_3\text{NH}_3\text{PbIBr}_2$ .

Blue photodetectors contained PEIE and different ratios of  $\text{PbI}_2$  and  $\text{PbBr}_2$  to tune the optical gap of  $\text{PbI}_x\text{Br}_{3-x}$ . Typically, 354 mg  $\text{PbI}_2$  and 121 mg  $\text{PbBr}_2$  were dissolved in DMF (1 ml) to create a 1.1 M  $\text{PbI}_{1.4}\text{Br}_{0.6}$  solution. A volume of 30  $\mu\text{l}$  of

the 5 wt% PEIE solution was added into 170  $\mu\text{l}$  of the  $\text{PbI}_{1.4}\text{Br}_{0.6}$  solution and stirred for 30 min. The PEIE: $\text{PbI}_{1.4}\text{Br}_{0.6}$  solution was spin-coated at 1,000 r.p.m. for 180 s to create the active layer.

After deposition, the active layers were heated at  $100^\circ\text{C}$  for 10 min on a hot plate in a nitrogen-filled glove box. Then, 60 nm of  $\text{C}_{60}$  was evaporated to form the hole-blocking layer to reduce the photodiode dark current. Finally, 1 nm of LiF and 100 nm of Ag were deposited by thermal evaporation under a  $10^{-6}$  mbar vacuum with an appropriate mask ( $0.2 \text{ cm}^2$  for each device) to form the cathode and complete the device. All photodiodes were encapsulated for device performance measurements. A standard encapsulation protocol was used: epoxy resin (XNR 5516Z-B1, Nagase ChemteX Corporation) was screened onto the edges of a capping glass plate, which was then placed onto the photodiodes firmly before being illuminated under ultraviolet light for 10 min.

**Characterization.** Optical absorption spectra were collected using a Cary 5000 UV-vis spectrophotometer and near normal incidence reflectance measurements were obtained using a FilmTek 2000 M TSV thin-film measurement system. The crystallinity of the films was characterized using XRD. All XRD spectra were obtained on a Bruker Advance D8 X-Ray Diffractometer equipped with a LynxEye detector, Cu tube ( $\text{CuK}\alpha = 1.5418 \text{ \AA}$ ) and operated at 40 kV with a  $2\theta$  scan range of  $10$ – $70^\circ$ . The surface morphology of the perovskite films and cross-sectional structure of the photodiodes were imaged using a Hitachi SU3500 SEM with an accelerating voltage of 10 keV and a Jeol JSM-7100F field-emission SEM (FESEM) (Jeol JSM-7100F) with an accelerating voltage of 2 keV. Film thicknesses were determined using a surface profilometer (Veeco Dektak 150). The capacitance of the devices was measured using the CELIV technique<sup>42</sup>.

**Device performance measurements.** The current density–voltage ( $J$ – $V$ ) characteristics were recorded using an Agilent B1500A Semiconductor Analyzer with a scan speed of  $0.01 \text{ V s}^{-1}$ . Light  $J$ – $V$  curves were recorded with NSPR510CS Nichia red LED (625 nm), 3 W high-power star emitter–green (520–530 nm) and blue (460–470 nm) illumination. EQE spectra and the near-normal incidence reflectance of the devices were recorded with a PV Measurements QEX7 system, which was calibrated with a NREL certified photodiode without light bias. Frequency response measurements were obtained using a NSPR510CS Nichia red LED (625 nm), a 3 W high power star emitter–green (520–530 nm) or a blue LED (460–470 nm)—modulated with an Agilent 33250A arbitrary waveform generator. The photocurrent responses of the photodiodes were recorded using a digital storage oscilloscope (LeCroy Waverunner A6200). LDRs were determined using laser diodes at 650 nm and 405 nm and a second-harmonic Nd:YAG laser (Laserver) operating continuously at 532 nm as the illumination source with a series of neutral density filters purchased from Thorlabs and Holmarc used to vary the light intensity. The light intensity was calibrated using a standard photodiode, simultaneously used to compensate for intensity fluctuations, and the current response was recorded using an Agilent B1500A Semiconductor Analyzer.